Sensitivity of Multislice Electron Ptychography to Point Defects: A Case Study in SiC

Aaditya Bhat, Colin Gilgenbach, Junghwa Kim, James LeBeau

[a] *Department of Materials Science and Engineering Massachusetts Institute of Technology Cambridge MA 02139 United States*

arXiv:2409.07663v1 [cond-mat.mtrl-sci] 11 Sep 2024

Abstract

Robust atomic resolution structural characterization of point defects in 3D is a longstanding challenge for electron microscopy. Here, we evaluate multislice electron ptychography as a tool to carry out 3D atomic resolution characterization of point defects in silicon carbide as a model. Through multislice electron scattering simulations, subsequent ptychographic reconstructions, and data analysis, we show that intrinsic defects such as vacancies and substitutions beyond transition metals can be detected with a depth precision of approximately 0.1 nm with realistic sample and microscope conditions. Furthermore, the dependence of contrast at defect sites on electron energy and dose, as well as optimal acquisition parameters, are described. Overall, these results serve as a guidepost to experiments aiming to analyze point defects beyond extremely thin specimens or only heavy elements.

1. Introduction

Color centers in silicon carbide (SiC) are a complex and rich class of point defects and defect complexes with optical and magnetic properties suitable for spin qubit applications [1]. First, silicon carbide is a technologically mature platform, making it an excellent potential host material. Second, single photon emitters formed from divacancies ($v_{Si}v_C$) or complexes of substitutions transition metal ions (v_{TM}) with carbon vacancies have been demonstrated to exhibit millisecond coherence times [2], emitting at telecom wavelengths [3], and provide high-fidelity electrical readout [4].

Because the electronic and magnetic interactions between the spin states of defects are strongly influenced by their geometry and their local environment [5], probes of their defect structures are helpful in guiding the design of new systems. However, the large variety of possible defects (intrinsic and extrinsic) and their multiple configurations present challenges for their characterization [6]. Conventionally, photoluminescence is used to distinguish these defects, but conclusive identification requires indirect magnetic measurements such as electron paramagnetic resonance (EPR) paired with density function theory (DFT) calculations [3, 1]. The limited spatial resolution of conventional methods, however, prevents direct determination of the atomic scale structure of point defects. For example, although chromium

Email address: lebeau@mit.edu (James LeBeau)

implantation induced defects ($Cr_{Si}vac_C$) can show high coherence times, near telecom band emission, and high-fidelity manipulations, their structure is unknown [7].

While atomic resolution high angle annular dark field scanning transmission electron microscopy (HAADF STEM) imaging has been shown to be sensitive to heavy dopants in 2D [8, 9] or 3D [10], very thin (<10 nm) samples are generally required. As a consequence, such investigations have proven to be extremely challenging and become essentially impossible with low defect concentrations (below 10^{19} cm^{-3}) or with low atomic number contrast (Si vs. V).

Recent advances in multislice electron ptychography (MEP), however, suggest that single point defect detection and quantification can be achieved with $\sim$3 nm depth resolution and in thicknesses up to above 40 nm [11, 12]. Multislice ptychography offers two primary advantages over ADF STEM for mapping defects. First, unlike HAADF STEM imaging, multislice ptychography can be used to image both heavy and light atoms simultaneously which is necessary to image point defects relevant to spin quantum computing. Second, depth resolution and incorporation of dynamical diffraction in reconstructions provides 3D information in relatively thicker samples where surface features can be well separated. The robust identification of defect complexes with MEP ptychography, however, requires that the defects be visible above a statically significant threshold and with depth resolution to connect the presence of vacancies in the proximity of dopant atoms [13]. Specifically, the sensitivity of multislice ptychography to point defects need to be established in the context of defect types, geometry and acquisition conditions.

In this article, we explore the detection of substitutional point defects and complexes in SiC using simulations and subsequent ptychographic reconstructions. First, the methods of processing and quantification of atomic resolution ptychographic reconstructions are described. Representative defect structures are considered for a variety of different microscope conditions including accelerating voltage, convergence angle, electron dose and acquisition parameters. The sensitivity of MEP to defect type and position are considered. Finally, we discuss how MEP can provide invaluable insights into color centers for quantum computing applications.

2. Methods

2.1. Structure Generation

Supercells of 4H SiC were oriented along $[10\bar{1}0]$ with dimensions of of 4.3 nm x 4.0 nm x 24.0 nm. The supercell dimensions were chosen to completely contain the electron probe within the projected area and with a thickness could be readily obtained through either focused ion beam or conventional preparation [8, 14]. Furthermore, this orientation was selected because the h and k sites of Si and C can be readily distinguished, as shown in Figure 1b. In addition, 2 nm of amorphous carbon was added to each surface of the structure to account for surface contamination.

Object phase at atomic sites show variations inherent to ptychographic reconstructions and hence structures chosen for simulation consist of arrays of kh and hh type X_{Si} v_C defect where X is a substitution or a vacancy. X is varied across vacancies and carbon antisite to

transition metal and heavier substitutions as discussed below. In simulations to investigate depth sensitivity and microscope parameter dependence, X is chosen to be vanadium which is associated with established spin active defects in SiC and by virtue of atomic number close to Si, is a suitable substitution to test limits of light dopant detection. An example structure of a defect array used to investigate microscope parameter dependence is shown in Figure 1.

2.2. Electron Scattering Simulations

Electron scattering simulations of 4D STEM datasets for ptychography were conducted using programs based on and validated against those developed by Kirkland [15]. Unless specified otherwise, simulations used a scan step of 50 pm, electron energy of 200 kV, 10 nm defocus, and a convergence semi-angle of 25 mrad. A diffraction pixel size of 1.0 mrad was used, to avoid padding diffraction patterns during reconstructions. Thermal vibrations were incorporated using the frozen phonon model [16] and 50 thermal configurations, with root mean square displacements of 5.3 and 5.4 pm for Si and C [17], respectively. The amorphous carbon layers were assigned thermal displacements of approximately 20 pm based on Ref. [18].

Noise and incoherence were incorporated into the simulation ptychography acquisitions. The point spread function reported for the detector [19] at 200 keV was applied to diffraction data prior to reconstruction. Subsequently, shot noise was added at each detector pixel considering a beam current of 20 pA and dwell time of 1 ms, unless otherwise stated. For the choice of scan step described above this corresponds to a dose of 50×10^7 e/nm^2.

2.3. Reconstructions

For ptychographic reconstructions, a modified version of the fold_slice [20, 21] fork of Ptychoshelves [22] was used. Least squares maximum likelihood iterative engine with GPU-acceleration [**?** **?** 23**?**] was used. 8 incoherent probe modes were used in all reconstructions to accommodate incoherence in multislice simulations. The reconstructions use a total object thickness of 24 nm composed of 1 nm slices. With the simulation parameters listed above, the reconstructed object had a nominal pixel size of 20 pm. For simulations with lower accelerating voltage, diffraction patterns were zero-padded before reconstruction to match this real space sampling.

In the simulations considered, due to contamination at the surfaces and a 2 nm depth resolution, a diffuse inhomogeneous background is seen in slices near the surface necessitating removal of 2 nm from top and bottom surfaces of the crystal. Such features are seen in experimental reconstructions as well [24]. Ptychography is insensitive to an affine phase ramp [25]. These are removed prior to analysis by linear detrending of each slice.

2.4. Data Analysis

Ptychographic reconstructions from gradient descent methods treat every pixel as a parameter and hence objects with least possible sampling converge most effectively. Accurate determination of phase in under sampled reconstructions can be done using various methods of up-sampling. Smoothing cubic spline interpolation is used here to up-sample all reconstructions and overcome noise with medium to high spatial frequencies.

Typical metrics to identify point defects include peak or integrated phase at each atom column location. Here, for simplicity, we use the peak phase as the metric to identify defects. The reconstructed object potential can contain differences in scaling and offsets in the potential depending on reconstruction parameters and true sample parameters. Consequently, comparing reconstructions across different datasets, and even those for a given dataset with different reconstruction parameters, can be challenging and require normalization.

Regardless of reconstruction parameters or metric, M, used, the difference in M for Si and C atom columns in a slice can be used as a reference for normalization as shown in Figure 2. Furthermore, scaling this difference by the atomic number difference between Si and C may enable comparing SiC to other materials and obtaining an "effective Z difference". Scaling by a factor of 8 is used here for the atomic number difference, but direct comparisons to other materials must account for non-linear Z contrast in ptychography described later. Changes in phase at either the Si or C site due to substitutions and vacancies can then be quantified with respect to this difference. This yields a natural definition for site contrast, χ to quantify phase at each site as:

$$\chi_{\text{site}} = \frac{M_{\text{site}} - \overline{M}_{\text{site}}}{(\overline{M}_{Si} - \overline{M}_{C})/8} \tag{1}$$

The standard deviation of the measured site contrast for silicon or carbon atom columns will depend on several factors such as dose, static displacements, and thermal vibrations. Using site contrast as defined above, the quality of reconstructions and choice of metrics can be evaluated by comparing standard deviations at Si or C sites. Based on these standard deviations a threshold can be chosen such that atom columns above or below it are identified as substitutional point defects.

3. Results and Discussion

3.1. Sensitivity to different defects

For kh and hh type X_{Si} v_c defect arrays considered for different substitutions X, site contrast varies as $Z^{0.68}$ with atomic number. As described above, site contrast at Si sites shows a standard deviation of 0.36, and for 99.5 % detection rate for defects assuming a Gaussian distribution, threshold for site contrast is ~ 1. The transmission function for defects is identical for all structures used for simulations, and hence, the reconstructed phase at substituted sites is expected to be similar for reconstructions up to variations due to noise. Hence a fixed threshold of 1 for Si sites is used as a reference for comparing sensitivity towards defect detection across all datasets. In experiment he threshold may be selected based on standard deviations of the dataset which depends on the quality of the sample and reconstruction.

From Figure 3, the electrically and spin inactive carbon antisites cannot be identified conclusively with a site contrast of -0.87. The silicon vacancy, a key intrinsic defect as an isolated vacancy and in a divacancy complex, shows a significantly higher magnitude in site contrast of -2.6. Among extrinsic defects with transition metal and heavier substitutions,

Vanadium was the lowest atomic number considered and is above the threshold for detection at 1.14. Heavier substituents such as molybdenum and erbium show a phase high enough to be discerned by visual inspection of an appropriately normalized slice phase. At the carbon sites, the standard deviation of sites is marginally lower than that for Si at 0.33, but the carbon vacancy, which is the key intrinsic defect, shows a low magnitude of site contrast due to a small atomic number difference. Here conclusive identification of individual defects is expected to be challenging.

In 4H SiC due to the ABAC stacking of Si and C layers sites can have neighborhood with hexagonal or cubic type symmetry. Along the $[1 0 \bar{1} 0]$ direction where Si and C atom columns are separated, nearest neighbors are tetrahedrally symmetric and in projection, a short and a long Si-C pair of distances are possible. This orientation is suitable for discerning between isolated defects and complexes. Site contrast for kh and hh configurations considered show that the lateral resolution of ptychography is sufficient to fully resolve both configurations spatially as well as retain independent object phase at all sites.

To enhance detection of intrinsic defects and relatively light substitutions, several microscope parameters can be optimized. Among these electron energy results in the most significant increase in site contrast. While decreased wavelength yields higher resolution, Si and C atom columns remain well resolved even at 80 kV. Reconstructions at 60 kV do not converge with parameters comparable to simulations considered here. At 80 kV mean contrast increases to 1.38 from 0.94 at 300 kV for the V_{Si} defect. Similarly, for smaller atomic number differences in intrinsic defects, imaging at 80 kV shows a higher site contrast compared to both 200 and 300 kV. This is expected from the increased interaction parameter which results in a more strongly scattering transmission function for the same potential. For higher atomic numbers, contrast at 80 kV is less than 200 kV but still higher than that for 300 kV. While this is likely due to dependence of the contrast transfer function on wavelength, a precise reason is not clear. At 300 kV identification of V_{Si} and intrinsic defects is difficult despite higher resolution. These results suggest that lower accelerating voltages to 80 kV are best suited for detection of defects despite reduced resolution.

3.1.1. Spatial mapping of defects in 3D

Distinguishing defects from surface features and mapping their positions in 3D is a key advantage of multislice ptychography over conventional 2D imaging methods. V_{Si} v_c type defects can be distinguished from isolated V_{Si} and v_c defects by estimating their proximity in depth. Provided each atom column has defect separation greater than the depth resolution, approximating their position depends on precision of measured depth. Since typically doping concentrations and formation energies for defect complexes are low, they are expected to be sufficiently separated within atom columns and reacting defects within 3 nearest neighbors are expected to be complexes. Hence, depth precision plays a more critical role compared to depth resolution.

Precision is measured here as the standard deviation of interpolated defect positions in depth about their true positions in the supercell. Smoothing cubic spline interpolation is used which accommodates asymmetry in the depth profiles in an atomic column about a defect. Depth resolution is measured here as the full width at half maximum of interpolated

site contrast depth profiles for a given atomic column. Despite a slice thickness of 1 nm, we find a depth precision of 0.094 nm, which is less than a unit cell in the $[10\bar{1}0]$ direction. While increasing convergence angle can increase depth resolution [23, 11], for point defects full width at half maximum does not appreciably change with convergence angle. Although depth resolution is subject to reconstruction slice thickness as well as acquisition parameters, here $\sim$2 nm is measured consistently for all convergence angles for a slice thickness of 1 nm.

3.1.2. Dependence on dose

Dose plays a multifaceted role in imaging and identification of point defects since it has an influence on structure of the sample while imaging as well as contributing to noise and hence affecting reconstruction of the acquired datasets. High doses, especially at higher electron energies, can induce defect generation as well as transformations such as migration and conversions. For SiC in particular 300 kV electrons have been used to create both silicon and carbon vacancies [26, 27]. The threshold for carbon vacancy generation has been reported to be approximately 150 kV [26, 28]. While reduction in electron energy provides a possible means to achieve lower beam damage, obtaining successful reconstructions is challenging. An alternative is to reduce electron dose, as is commonly done for beam sensitive samples. Atomic resolution multislice ptychography is particularly challenging because of the small scan step sizes typically used for high quality reconstructions, leading to higher doses at the same beam current. Reducing beam current is possible, but leads to fewer incident electrons in a diffraction pattern and consequently higher Poisson noise.

In simulations here, beam current ranging from 0.625 pA to 80 pA are considered with a dwell time of 1 ms (based on EMPAD1 4D STEM detector). Dose is calculated as incident electrons in a unit of the scan grid. This is independent of defocus and is representative of actual dose when defocus is sufficiently smaller than the field of view. For a scan step of 0.5 A, dose ranges from 1.5–200 $\times$ 10^7 e/nm^2 with each diffraction pattern receiving approximately 4×10^3 to 5×10^5 incident electrons. With the detector parameters used here, this results in pixels in the bright field disc receive an average of ¡10 electrons at the lowest dose considered. At doses above 25×10^7 e/nm^2, mean site contrast shows a small change of 7% (from 1.27 to 1.36) approaching a dose of 200×10^7 e/nm^2. Below the lower limit, reconstructions show distinct Si and C atom columns, but the standard deviation of defect site contrast increases above 0.5 and $> 10\%$ of defects are not identified. At the lowest dose considered point defect detection is not possible for vanadium.

3.1.3. Optimizing acquisition parameters for defect detection

Simulations considered above fix acquisition parameters, specifically defocus and scan step. These are known to influence quality of reconstructions [29] in a coupled manner quantified through the dimensionless metrics of Ronchigram magnification and areal oversampling. Increased Ronchigram magnification resulting from decreasing defocus shows an increased sensitivity to defects as mean site contrast for V_{Si} increases by 16% (from 1.24 to 1.44) as defocus is varied from 20 nm to 5 nm. Varying areal oversampling on the other shows only small changes in mean site contrast for converged reconstructions. At a high scan step of 0.083 nm and for low defocus of 5 nm, area oversampling is insufficient for the

reconstruction to converge with the fixed set of reconstruction parameters used. In practice, defocus is typically estimated from virtual images from the 4D STEM acquisition as well as estimating it using feature sizes in the Ronchigram. It is not always possible to obtain accurate estimates of the defocus and at high scan steps there is a possibility of acquiring data with low area oversampling. Hence, a defocus of 7-12 nm and a scan step of 0.05 nm is suitable for reliable ptychographic acquisitions.

4. Conclusion

Using multislice electron ptychography, the identification of a wide variety of point defects in SiC is possible. However, careful selection of imaging and microscope parameters, as well data analysis methods specific to ptychographic reconstructions, is required. Among imaging parameters defocus and scan step are crucial to obtain highest contrast at defect sites. Probe convergence angle has a relatively limited influence on contrast above a threshold for effective reconstructions. Energy and electron dose are key microscope parameters considered. Contrast, but not resolution, increases when energy is reduced which is also beneficial in reducing beam induced damage. Electron dose has a limited effect on site contrast similar to convergence angle.

The results indicate that while antisites and carbon vacancies may not be possible to detect conclusively, silicon vacancies and substitutions as light as vanadium, which are relevant for quantum applications, can be detected reliably. For defect complexes, the estimated depth precision of ~ 0.1 nm is sufficient to discern them from isolated defects and provide 3D spatial distributions. Hence, for complex systems such as in SiC, MEP provides a compelling avenue to resolve structures of elusive spin active defects, and address the longstanding challenge of robust single substitution detection beyond extremely thin samples with heavy dopants. This sets the stage for investigations into local structures at and around point defects to reveal the origins of their unique properties and dynamics, hitherto inaccessible through conventional TEM imaging methods.

Acknowledgements

The authors acknowledge support from the Air Force Office of Scientific Research (FA9550-22-1-0370). This work was performed with the assistance of MIT SuperCloud and was carried out in part through the use of MIT's Characterization.nano facilities. Data processing was carried out in part using the cSAXS ptychography MATLAB package developed by the Science IT and the coherent X-ray scattering (CXS) groups, Paul Scherrer Institut, Switzerland. The version of this package used contains modifications and improvements by Zhen Chen, Yi Jiang, as well as the authors.

References

[1] S. Castelletto, A. Boretti, Silicon carbide color centers for quantum applications, J. Phys. Photonics 2 (2) (2020) 022001.

[2] D. J. Christle, A. L. Falk, P. Andrich, P. V. Klimov, J. U. Hassan, N. T. Son, E. Janzén, T. Ohshima, D. D. Awschalom, Isolated electron spins in silicon carbide with millisecond coherence times, Nat. Mater. 14 (2) (2015) 160–163.

[3] G. Wolfowicz, F. J. Heremans, C. P. Anderson, S. Kanai, H. Seo, A. Gali, G. Galli, D. D. Awschalom, Quantum guidelines for solid-state spin defects, Nature Reviews Materials 6 (10) (2021) 906–925.

[4] C. P. Anderson, E. O. Glen, C. Zeledon, A. Bourassa, Y. Jin, Y. Zhu, C. Vorwerk, A. L. Crook, H. Abe, J. Ul-Hassan, T. Ohshima, N. T. Son, G. Galli, D. D. Awschalom, Five-second coherence of a single spin with single-shot readout in silicon carbide, Science Advances 8 (5) (2022) eabm5912.

[5] F. Dolde, I. Jakobi, B. Naydenov, N. Zhao, S. Pezzagna, C. Trautmann, J. Meijer, P. Neumann, F. Jelezko, J. Wrachtrup, Room-temperature entanglement between single defect spins in diamond, Nat. Phys. 9 (3) (2013) 139–143.

[6] M. Bockstedte, A. Mattausch, O. Pankratov, Ab initio study of the migration of intrinsic defects in -SiC, Phys. Rev. B Condens. Matter 68 (20) (2003) 205201.

[7] B. Diler, S. J. Whiteley, C. P. Anderson, G. Wolfowicz, M. E. Wesson, E. S. Bielejec, F. Joseph Heremans, D. D. Awschalom, Coherent control and high-fidelity readout of chromium ions in commercial silicon carbide, npj Quantum Information 6 (1) (2020) 1–6.

[8] P. M. Voyles, J. L. Grazul, D. A. Muller, Imaging individual atoms inside crystals with ADF-STEM, Ultramicroscopy 96 (3-4) (2003) 251–273.

[9] H. Kim, J. Y. Zhang, S. Raghavan, S. Stemmer, Direct observation of sr vacancies in $SrTiO_3$ by quantitative scanning transmission electron microscopy, Phys. Rev. X 6 (4) (2016) 041063.

[10] R. Ishikawa, N. Shibata, T. Taniguchi, Y. Ikuhara, Three-dimensional imaging of a single dopant in a crystal, Phys. Rev. Appl. 13 (3) (2020) 034064.

[11] Z. Chen, Y.-T. Shao, Y. Jiang, D. Muller, Three-dimensional imaging of single dopants inside crystals using multislice electron ptychography, Microanal 27 (S1) (2021) 2146–2148.

[12] Z. Dong, M. Huo, J. Li, J. Li, P. Li, H. Sun, L. Gu, Y. Lu, M. Wang, Y. Wang, Z. Chen, Visualization of oxygen vacancies and self-doped ligand holes in La3Ni2O7-δ, Nature (2024) 1–6.

[13] C. Zhang, F. Gygi, G. Galli, Engineering the formation of spin-defects from first principles, Nat. Commun. 14 (1) (2023) 5985.

[14] Z. Chen, Y.-T. Shao, S. E. Zeltmann, H. K. P., E. R. Rosenberg, C. A. Ross, Y. Jiang, D. A. Muller, Imaging interstitial atoms with multislice electron ptychography, arXiv [cond-mat.mtrl-sci] (Jul. 2024).

[15] E. J. Kirkland, Advanced computing in electron microscopy, 2nd Edition, Springer, New York, NY, 2010.

[16] R. F. Loane, P. Xu, J. Silcox, Thermal vibrations in convergent-beam electron diffraction, Acta Crystallogr. A 47 (3) (1991) 267–278.

[17] J. S. Reid, Debye–Waller factors of zinc-blende-structure materials – a lattice dynamical comparison, Acta Crystallogr. A 39 (1) (1983) 1–13.

[18] M. Müllner, J. Maetz, H. Jex, Thermal diffuse scattering from pyrolytic graphite investigated with {M}össbauer γ-ray diffraction, Physica Status Solidi A Appl. Res. 56 (2) (1979) 541–544.

[19] M. W. Tate, P. Purohit, D. Chamberlain, K. X. Nguyen, R. Hovden, C. S. Chang, P. Deb, E. Turgut, J. T. Heron, D. G. Schlom, D. C. Ralph, G. D. Fuchs, K. S. Shanks, H. T. Philipp, D. A. Muller, S. M. Gruner, High dynamic range pixel array detector for scanning transmission electron microscopy, Microsc. Microanal. 22 (1) (2016) 237–249.

[20] Z. Chen, Y. Jiang, Y.-T. Shao, M. E. Holtz, M. Odstrčil, M. Guizar-Sicairos, I. Hanke, S. Ganschow, D. G. Schlom, D. A. Muller, Electron ptychography achieves atomic-resolution limits set by lattice vibrations, Science 372 (6544) (2021) 826–831.

[21] Y. Jiang, fold_slice: Electron/X-ray ptychography and tomography/laminography.

[22] K. Wakonig, H.-C. Stadler, M. Odstrčil, E. H. R. Tsai, A. Diaz, M. Holler, I. Usov, J. Raabe, A. Menzel, M. Guizar-Sicairos, PtychoShelves, a versatile high-level framework for high-performance analysis of ptychographic data, J. Appl. Crystallogr. 53 (2) (2020) 574–586.

[23] E. H. R. Tsai, I. Usov, A. Diaz, A. Menzel, M. Guizar-Sicairos, X-ray ptychography with extended depth of field, Opt. Express 24 (25) (2016) 29089.

[24] S. Karapetyan, S. Zeltmann, T.-K. Chen, V. D. H. Hou, D. A. Muller, Visualizing defects and amorphous materials in 3D with mixed-state multislice electron ptychography, Microsc. Microanal. 30 (Supplement_1) (Jul. 2024).

[25] A. Fannjiang, Raster grid pathology and the cure, Multiscale Model. Simul. 17 (3) (2019) 973–995.

[26] H. J. von Bardeleben, J. L. Cantin, L. Henry, M. F. Barthe, Vacancy defects in p-type 6H-SiC created by low-energy electron irradiation, Phys. Rev. B Condens. Matter 62 (16) (2000) 10841–10846.

[27] F. C. Beyer, C. Hemmingsson, H. Pedersen, A. Henry, E. Janzén, J. Isoya, N. Morishita, T. Ohshima, Annealing behavior of the EB-centers and M-center in low-energy electron irradiated *n*-type 4H-SiC, J. Appl. Phys. 109 (10) (May 2011).

[28] T. Knežević, A. Hadžipašić, T. Ohshima, T. Makino, I. Capan, M-center in low-energy electron irradiated $4H$-SiC, Appl. Phys. Lett. 120 (25) (Jun. 2022).

[29] C. Gilgenbach, X. Chen, J. M. LeBeau, A methodology for robust multislice ptychography, Microsc Microanal (2024) ozae055.

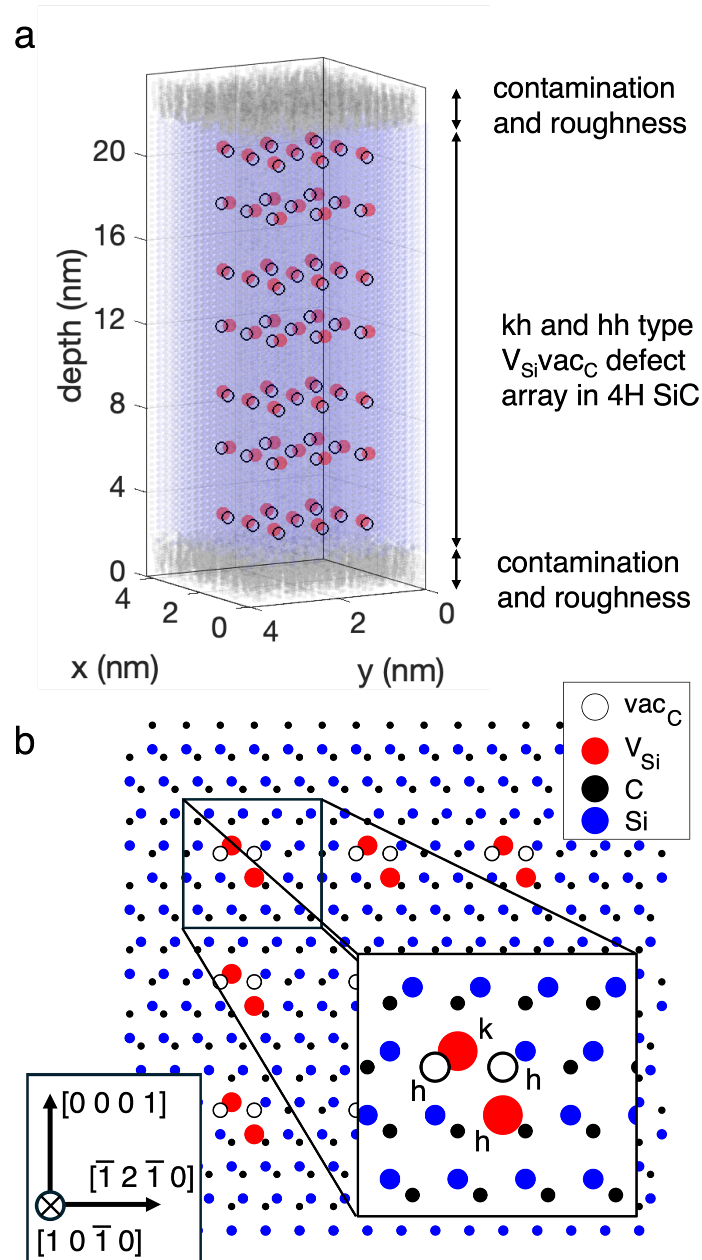

Figure 1: (a) Representative supercell containing an array of $V_{Si}vac_C$ defects and with surface roughness/carbon contamination. (b) *kh* and *hh* configurations viewed along the $[1\,0\,\bar{1}\,0]$ orientation of 4H SiC.

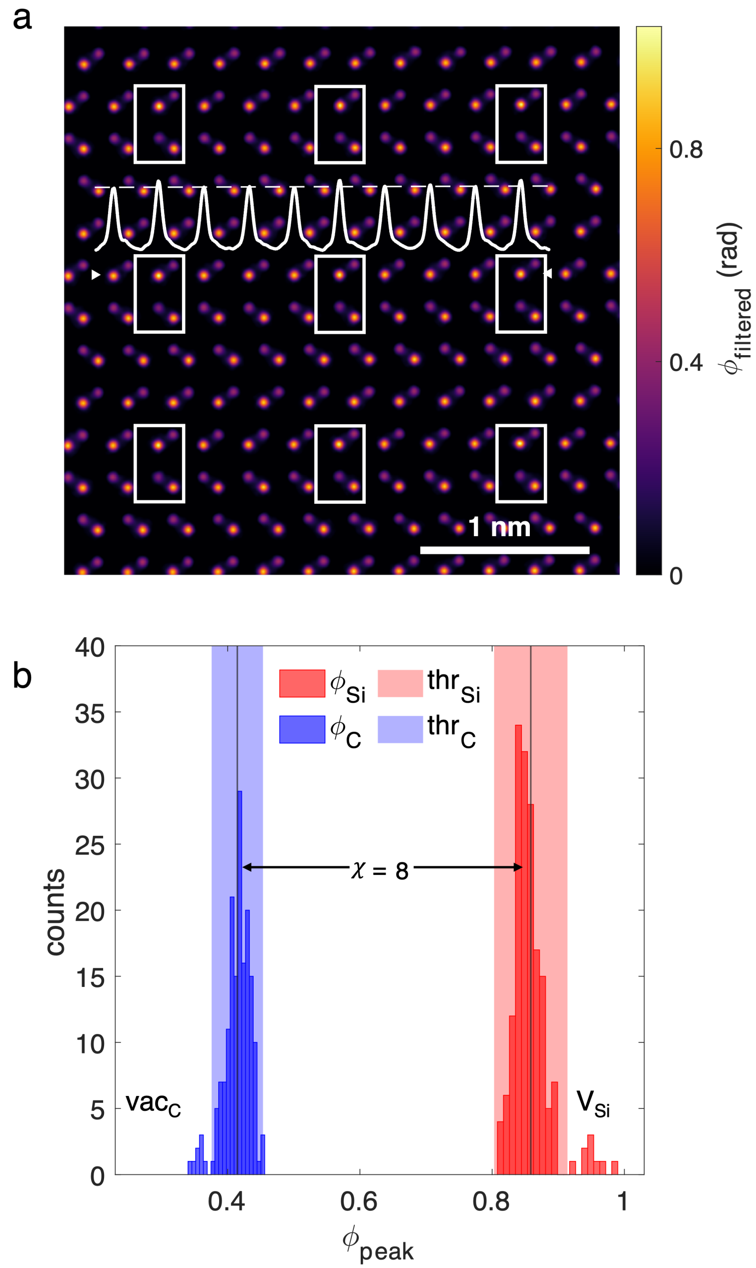

Figure 2: Collective histogram of peak Si and C site phases in a slice containing an array of hh type $V_{\mathrm{Si}}\mathrm{vac}_{\mathrm{C}}$ defects. The peak object phase at defect sites that lie beyond the indicated thresholds and the difference between mean Si and C phases used for normalization to obtain site contrast are indicated.

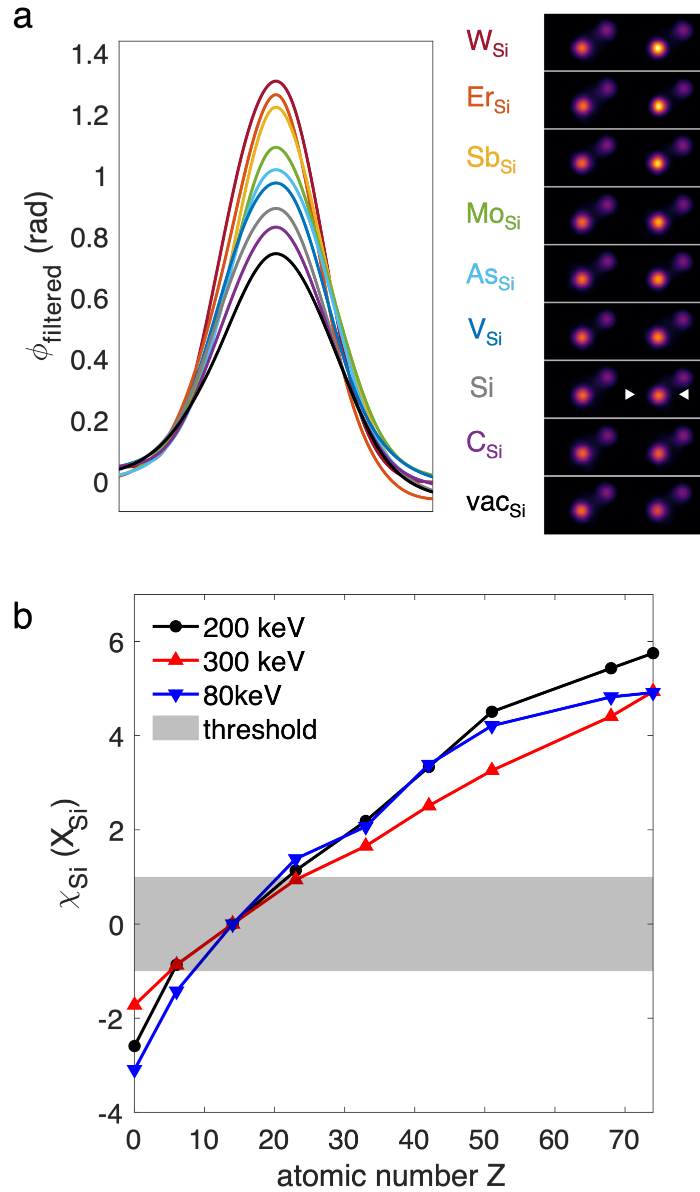

Figure 3: (a) Line profiles across defect sites containing intrinsic and extrinsic substitutions show increasing peak phase with atomic number and (b) variation of atomic number dependence of site contrast with electron accelerating voltage.

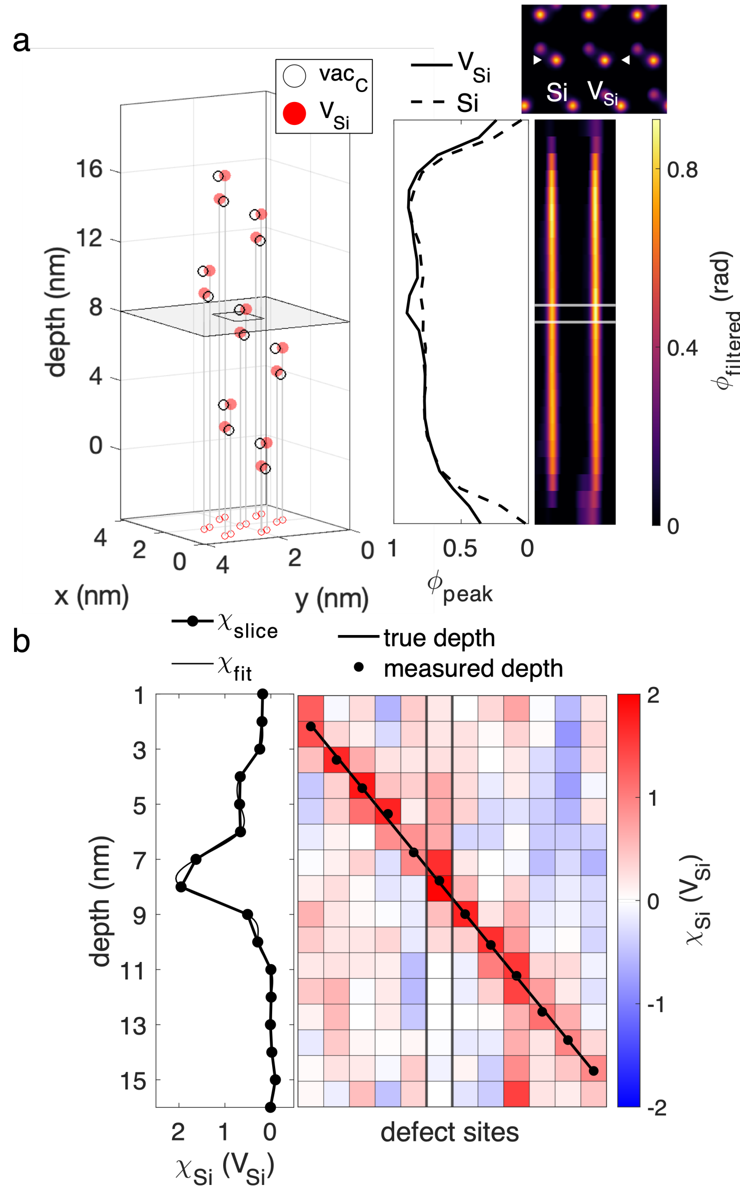

Figure 4: a) Schematic of the array of $V_{Si}vac_C$ defects at various depths and an example cross section of the reconstructed multislice phase object through depth and across a line containing neighboring Si columns with and without a vanadium substitution. (b) Site contrast variation through depth at defect sites showing the true position in the structure compared to measured position in depth. Measured position is estimated using smoothing cubic spline interpolation with an example fit shown at the highlighted defect column.

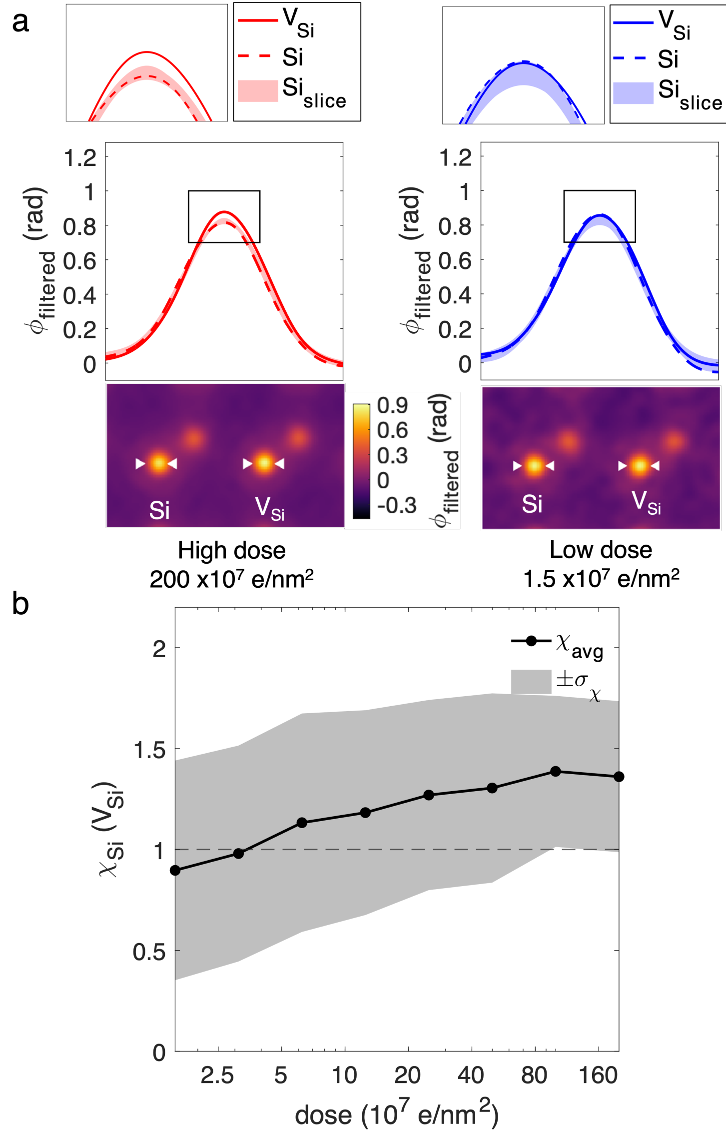

Figure 5: (a) Reconstructed phase and line profiles across neighboring Si sites with and without V_{Si} defects at a low (1.5×10^7 e/nm^2) and high dose (200×10^7 e/nm^2). Variation of phase across Si sites is shown for reference. (b) Mean site contrast at defect sites decreases in magnitude sharply at low doses as seen in the variation of site contrast with dose (dose shown with a log scale).

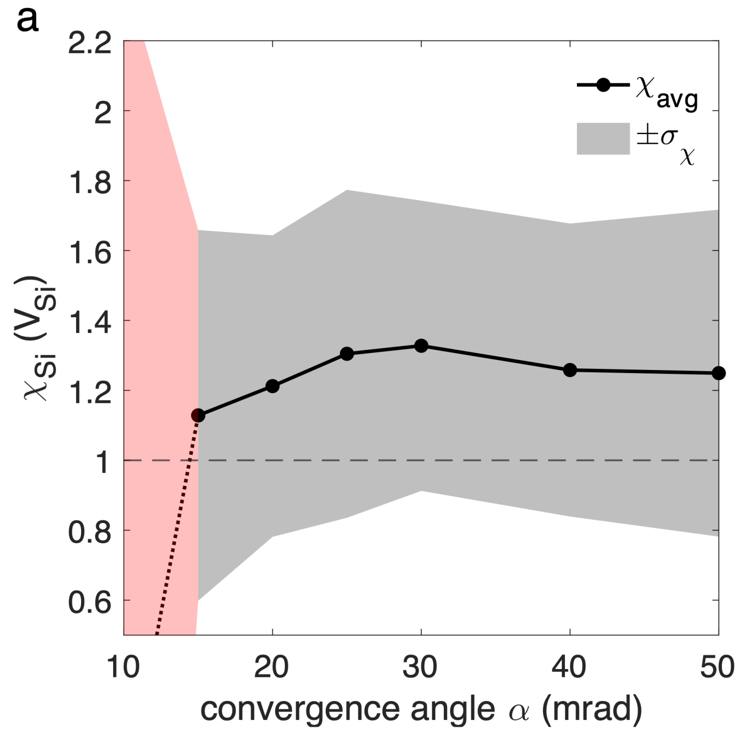

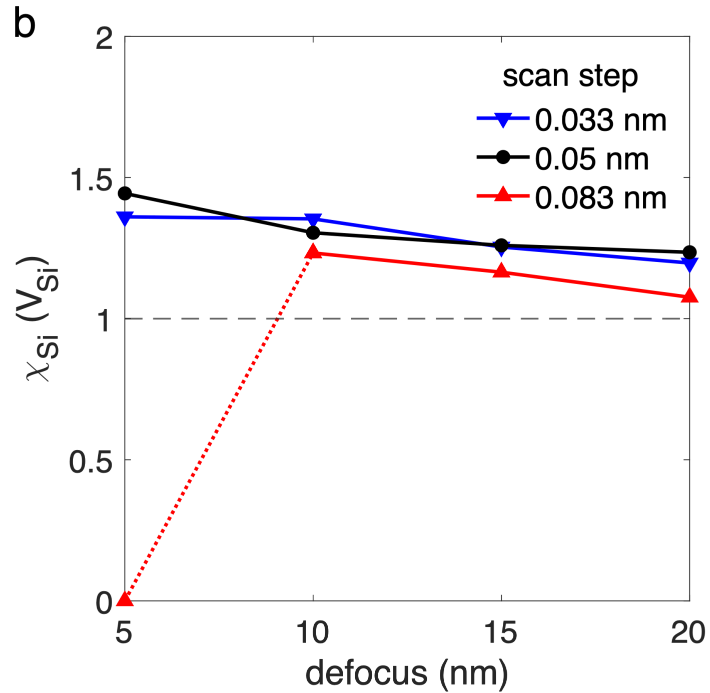

Figure 6: (a) Variation of mean V_{Si} site contrast with convergence angle. Sharp decrease in mean site contrast and increase in standard deviation is seen with a probe semi angle of 10 mrad. (b) Variation of mean V_{Si} site contrast with defocus shows negligible change with scan step except at high scan steps and low defocus where reconstructions fail due to low area oversampling.